Hydrothermal Synthesis of Lanthanide Fluorides LnF₃ (Ln = La to Lu) Nano-/Microcrystals with Multiform Structures and Morphologies

Chunxia Li, Jun Yang, Piaoping Yang, Hongzhou Lian, and Jun Lin*

State Key Laboratory of Rare Earth Resource Utilization, Changchun Institute of Applied Chemistry, Chinese Academy of Sciences, Changchun 130022, People's Republic of China, and Graduate University of the Chinese Academy of Sciences, Beijing 100049, People's Republic of China

Lanthanide fluoride LnF_3 (Ln = La to Lu) nano-/microcrystals with multiform crystal structures (hexagonal and orthorhombic) and morphologies (separated elongated nanoparticles, aggregated nanoparticles, polyhedral microcrystals) were successfully synthesized by a facile, effective, and environmentally friendly hydrothermal method. X-ray diffraction, Fourier transform infrared spectroscopy, scanning electron microscopy, transmission electron microscopy, high-resolution transmission electron microscopy, and photoluminescence spectra were used to characterize the samples. The experimental results indicated that the use of $NaBF_4$ is indispensable for obtaining LnF_3 crystal structures. Furthermore, the organic additive trisodium citrate (Cit^{3-}) has an obvious impact on the morphologies of the products to some degree. The possible formation mechanisms for LnF_3 nano-/microcrystals are presented in detail. Additionally, we systematically investigated the luminescence properties of the LnF_3:Eu^{3+} (Ln = La, Gd, and Lu) samples and found an efficient energy transfer from Gd^{3+} to Eu^{3+} in GdF_3:Eu^{3+}.

Introduction

In modern chemistry and materials science, the precise architectural manipulation of nanocrystals (NCs) with well-defined morphologies and accurately tunable sizes remains a research focus and a challenging issue because it is well-known that the properties of the materials closely interrelate with geometrical factors such as shape, dimensionality, and size.[1] Thus far, dramatic efforts have been dedicated to develop new methods for the fabrication of a range of high-quality inorganic nanostructures in different systems. From the perspective of application, nanomaterials are not only synthesized in large quantities with a desired composition, reproducible size, shape, and structure but also are prepared and assembled using green, environmentally responsible methodologies. As such, the development of a mild and more controlled method for creating such novel architectures will be of general interest. Recently, environmentally friendly synthetic methodologies that include molten-salt synthesis, hydrothermal processing, and template synthesis have gradually been implemented as viable techniques in the synthesis of a range of nanostructures.[2] Especially the hydrothermal method as a typical solution-based approach has been proven to be an effective and convenient process in preparing various

inorganic materials with diverse controllable morphologies and architectures.[3] Environmentally acceptable advantages of this method include easily controllable reaction conditions, relatively large scale and high yield in terms of the quantity of desired products, as well as frequently using water as the reaction medium. Our group successfully synthesized hexagonal $NaYF_4$ microcrystals with uniform hexagonal prism, disk, tube, rod, and octadecahedral shapes via a facile hydrothermal route.[4]

Because of their unique electronic, optical, and chemical characteristics arising from the 4f electrons, binary fluoride LnF_3 nano- and microstructures, a category of important rare earth fluoride compounds, have attracted increasing attention because of their potential applications in optics, optoelectronics, and particularly for the fluorescent labeling of cells.[5] Although LnF_3 crystals with various morphologies have been successfully synthesized,[6] there are few papers that have reported on the general preparation of LnF_3 nano-/microc-

* Corresponding author. E-mail: jlin@ciac.jl.cn.

(1) (a) Alivisatos, A. P. *Science (Washington, DC, U.S.)* **1996,** *271,* 933. (b) Ding, Y.; Yu, S. H.; Liu, C.; Zang, Z. A. *Chem.—Eur. J.* **2007,** *13,* 746. (c) Hu, J.; Odom, T. W.; Lieber, C. M. *Acc. Chem. Res.* **1999,** *32,* 435. (d) Markovich, G.; Collier, C. P.; Henrichs, S. E.; Remacle, F.; Levine, R. D.; Heath, J. R. *Acc. Chem. Res.* **1999,** *32,* 415.

(2) (a) Zhou, H.; Mao, Y.; Wong, S. S. *Chem. Mater.* **2007,** *19,* 5238. (b) Mao, Y. B.; Park, T. J.; Zhang, F.; Zhou, H. J.; Wong, S. S. *Small* **2007,** *3,* 1122.

(3) (a) Wang, L. Y.; Li, Y. D. *Nano Lett.* **2006,** *6,* 1645. (b) Liang, J. H.; Peng, Q.; Wang, X.; Zheng, X.; Wang, R. J.; Qiu, X. P.; Nan, C. W.; Li, Y. D. *Inorg. Chem.* **2005,** *44,* 9405. (c) Mao, Y.; Wong, S. S. *J. Am. Chem. Soc.* **2006,** *128,* 8217. (d) Song, R. Q.; Xu, A. W.; Yu, S. H. *J. Am. Chem. Soc.* **2007,** *129,* 4152.

(4) (a) Li, C. X.; Yang, J.; Quan, Z. W.; Yang, P. P.; Kong, D. Y.; Lin, J. *Chem. Mater.* **2007,** *19,* 4933. (b) Li, C. X.; Quan, Z. W.; Yang, J.; Yang, P. P.; Lin, J. *Inorg. Chem.* **2007,** *46,* 6329.

(5) (a) Lage, M. M.; Righi, A.; Matinaga, F. M.; Gesland, J.-Y.; Moreira, R. L. *J. Phys.: Condens. Matter* **2004,** *16,* 3207. (b) Stouwdam, J. W.; van Veggel, F. C. J. M. *Nano Lett.* **2002,** *2,* 733. (c) Chen, D. Q.; Wang, Y. S.; Zheng, K. L.; Guo, T. L.; Yu, Y. L.; Huang, P. *Appl. Phys. Lett.* **2007,** *91,* 251903.

(6) (a) Lemyre, J. L.; Ritcey, A. M. *Chem. Mater.* **2005,** *17,* 3040. (b) Tao, F.; Wang, Z. J.; Yao, L. Z.; Cai, W. L.; Li, X. G. *J. Phys. Chem. C* **2007,** *111,* 3241. (c) Liu, C. H.; Chen, D. P. *J. Mater. Chem.* **2007,** *17,* 3875. (d) Zhang, Y. W.; Sun, X.; Si, R.; You, L. P.; Yan, C. H. *J. Am. Chem. Soc.* **2005,** *127,* 3260. (e) Yan, R. X.; Li, Y. D. *Adv. Funct. Mater.* **2005,** *15,* 763.

rystals via a facile and effective method. Yan's group reported the synthesis of LnF$_3$ nanocrystals with a single source approach for utilizing the surfactant with high-temperature solvents.[7] This method is based on the thermo-decomposition of rare earth trifluoroacetates in organic solvents, which needs stringent experimental conditions (~300 °C, waterless, oxygen-free, and inert gas protection). In addition, a general liquid–solid solution (LSS) methodology provided by Li's group was used to prepare a whole group of rare earth fluoride nanocrystals, the success of which depends upon the effective complexation of linoleate on the surfaces of nanocrystals in a water−ethanol mixed-solution system.[8] In this process, highly toxic NH$_4$HF$_2$ is used as the fluorine source for the synthesis of YbF$_3$ and YF$_3$, and the synthetic procedures are a little more complicated, especially the post-treatment process. As such, the discovery and exploitation of a green, facile, and general method to systematically prepare LnF$_3$ nano-/microstructures is urgently required. On the other hand, for lanthanide fluorides, because NaF or NaBF$_4$ is usually used as the fluorine source, Na$^+$ can be incorporated into the framework of Ln−F, resulting in the formation of complex NaLnF$_4$. Accordingly, it is difficult to control the compositions of the products.

Herein, in this paper, we demonstrate a general strategy for the synthesis of LnF$_3$ nano-/microstructures via a hydrothermal route. More importantly, we can easily control the composition of the products through the elaborate choice of fluorine source, namely, that LnF$_3$ is achieved using NaBF$_4$ as the fluorine source. The structure, formation mechanism, and photoluminescence (PL) properties of products also were investigated in detail.

Experimental Procedures

Preparation. The lanthanide oxides Ln$_2$O$_3$ (except for Tb and Ce elements) (99.999%) and Tb$_4$O$_7$ (99.999%) as well as Ce(NO$_3$)$_3$·6H$_2$O were purchased from the Science and Technology Parent Company of the Changchun Institute of Applied Chemistry, and other chemicals were purchased from the Beijing Chemical Company. All chemicals were analytical grade reagents and used without further purification. The lanthanide chloride stock solutions of 0.2 M were prepared by dissolving the corresponding metal oxide in hydrochloric acid at elevated temperatures. In a typical procedure for the preparation of LaF$_3$ nanoparticles, 10 mL of LaCl$_3$ (0.2 M) was added to 20 mL of aqueous solution containing 2 mmol of trisodium citrate (Cit^{3-}) to form the La−Cit^{3-} complex. After vigorous stirring for 30 min, 30 mL of aqueous solution containing 25 mmol of NaBF$_4$ was introduced into the solution. The pH of the mixture was adjusted to 1 with diluted HCl (1 M). After additional agitation for 15 min, the as-obtained mixing solution was transferred into a Teflon bottle held in a stainless steel autoclave, sealed, and maintained at 180 °C for 24 h. As the autoclave cooled to room temperature naturally, the precipitates were separated by centrifugation, washed with ethanol and deionized water in sequence, and then dried in air at 80 °C for 12 h. Other LnF$_3$ (Ce−Lu) or Eu^{3+}-doped LnF$_3$ (La, Gd, and Lu) samples were prepared by a similar procedure. Additionally, different hydrother-
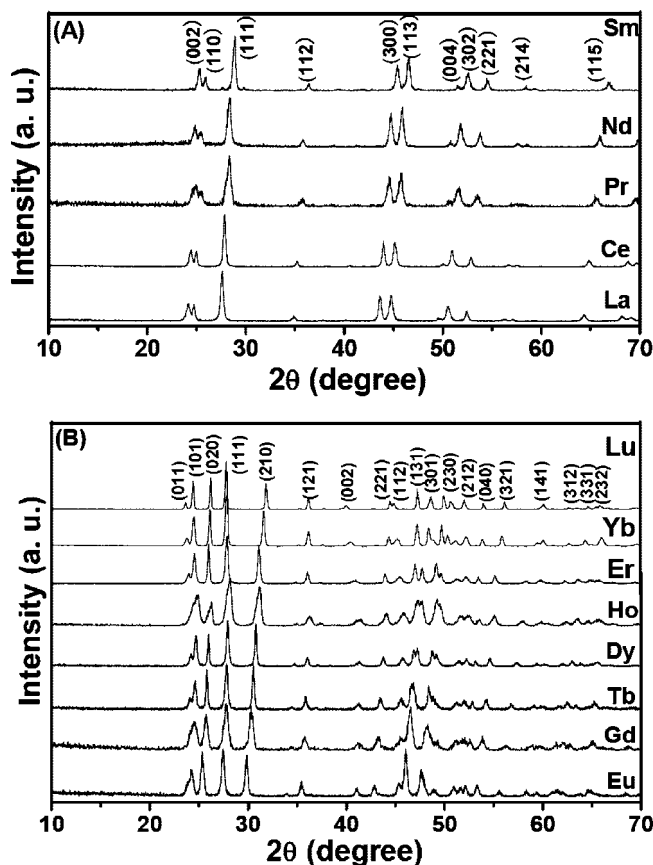
Figure 1. XRD patterns of as-prepared LnF$_3$ products. (A) XRD patterns of LnF$_3$ (Ln = La to Sm) with a hexagonal crystal structure and (B) XRD patterns of LnF$_3$ (Ln = Eu to Lu) with an orthorhombic crystal structure.

mal treatment times at 180 °C were selected to investigate the morphological evolution process of EuF$_3$ and TbF$_3$ products.

Characterizations. X-ray powder diffraction (XRD) measurements were performed on a Rigaku-Dmax 2500 diffractometer at a scanning rate of 8°/min in the 2θ range from 10 to 70°, with graphite monochromatized Cu Kα radiation (λ = 0.15405 nm). Infrared spectra were measured on a Vertex 70 FT-IR spectrophotometer (Bruker) with the KBr pellet technique. SEM micrographs were obtained using field emission scanning electron microscopy (FE-SEM, XL30, Philips). Low- to high-resolution TEM was performed using FEI Tecnai G2 S-Twin with a field emission gun operating at 200 kV. Images were acquired digitally on a Gatan multiople CCD camera. The PL excitation and emission spectra were recorded with a Hitachi F-4500 spectrophotometer equipped with a 150 W xenon lamp as the excitation source. All measurements were performed at room temperature.

Results and Discussion

Structures. Lanthanide atoms have close and gradually changed ionic radii, and as a result, the physical and chemical properties change correspondingly. Previous studies on lanthanide hydroxides, phosphates, and orthovanadates indicate that the crystal structures and morphologies change gradually with decreasing ionic radii.[9] In our case, by means

(7) Sun, X.; Zhang, Y. W.; Du, Y. P.; Yan, Z. G.; Si, R.; You, L. P.; Yan, C. H. *Chem.—Eur. J.* **2007**, *13*, 2320.

(8) Wang, X.; Zhuang, J.; Peng, Q.; Li, Y. D. *Inorg. Chem.* **2006**, *45*, 6661.

(9) (a) Wang, X.; Li, Y. D. *Angew. Chem., Int. Ed.* **2002**, *41*, 4790. (b) Huo, Z. Y.; Chen, C.; Chu, D. R.; Li, H. H.; Li, Y. D. *Chem.—Eur. J.* **2007**, *13*, 7708. (c) Liu, J. F.; Li, Y. D. *J. Mater. Chem.* **2007**, *17*, 1797.

Hydrothermal Synthesis of LnF₃ (Ln = La−Lu)

Chem. Mater., Vol. 20, No. 13, 2008 4319

Table 1. Summary of Crystal Structures, Space Groups, JCPDS Numbers, Morphologies, Sizes, and Average Crystallite size (*D*) of LnF₃ Crystals

LnF₃	crystal phase	space group	JCPDS	morphology	length (nm)	diameter (nm)	D (nm) from XRD
La	hexagonal	$P\bar{3}c1$	32-0483	elongated nanoparticles	42	20	16.2
Ce		$P6_3/mcm$	08-0045		40	24	31.6
Pr		$P\bar{3}c1$	46-1167		34	15	18.1
Nd		$P6_3/mcm$	09-0416		56	38	21.8
Sm		$P6_3/mcm$	12-0792		150	80	28.8
Eu	orthorhombic	$Pnma$	33-0542	aggregates consisting of nanoparticles		560	22.6
Gd			12-0788		406	200	16.8
Tb			37-1487		600	347	25.6
Dy			32-0352		920	760	28.4
Ho			23-0284		760	126	15.2
Er			32-0361		945	428	27.2
Yb			34-0102	octahedra	350		
Lu			32-0612		300−1000		

of the XRD technique, the as-prepared LnF₃ products under similar synthetic conditions adopt two different kinds of crystal structures, as shown in Figure 1. All diffraction peaks shown in Figure 1A can be indexed easily as the pure, hexagonal phase of LnF₃ (from La to Sm), among which LaF₃ and PrF₃ have a $P\bar{3}c1$ space group; otherwise, CeF₃, NdF₃, and SmF₃ have a $P6_3/mcm$ space group. Because of the smaller size of the products, the pattern is apparently broadened. On the contrary, with smaller Ln³⁺ ions (from Eu to Lu), as-obtained LnF₃ adopts an orthorhombic crystal phase with the space group $Pnma$, as presented in Figure 1B. The intensities and positions of the peaks of all samples are in accordance with literature data (see JCPDS nos. of Table 1). These results indicate that the completely crystalline and pure-phase lanthanide fluorides LnF₃ could be obtained by using this facile hydrothermal treatment. Although the exact reason for this phenomenon is not very clear, the variation of crystal structures seems to be closely related to the gradual radius contraction of Ln³⁺. A similar result has been reported by Wang and co-workers.[8]

FT-IR Spectrum. To further examine the purity of LnF₃ products, the FT-IR spectroscopy was performed by using LaF₃ as a representative example (Figure S1, Supporting Information). It can be clearly seen that all peaks can be ascribed to the characteristic adsorptions of the organic additive trisodium citrate (Na₃C₆H₅O₇·2H₂O, labeled as Cit³⁻). It seems that no peaks of oxo-species such as Ln−O bond vibration are present in the FT-IR spectrum (which is quite different from the case of Ln₂O₃ reported previously[10]). The broad absorption band at 3425 cm⁻¹ is ascribed to the O−H stretching vibration. The 2931 and 2850 cm⁻¹ transmission bands are assigned to the asymmetric (ν_{as}) and symmetric (ν_s) stretching vibrations of methylene (CH₂) in the Cit³⁻ molecule, respectively. The peak at 1720 cm⁻¹ is attributed to the C=O stretching vibration frequency. The bands at 1623 and 1422 cm⁻¹ also can be assigned to the asymmetric (ν_{as}) and symmetric (ν_s) stretching vibrations of the carboxylic group (-COO⁻), respectively.[3a,10a] Although the as-prepared sample was washed several times with water and ethanol, there were still some organic molecules Cit³⁻ on the surface of the particles.

Morphologies. Although the crystal structures of LnF₃ are only hexagonal and orthorhombic, the growth habits of the

crystals are more complicated. According to the difference of crystal phases and morphologies, the whole growth regions can be classified into three distinct groups of La−Sm, Eu−Er, and Yb−Lu. Table 1 summarizes crystal structures, space groups, JCPDS numbers, morphologies, sizes, and the average crystallite size (D) calculated from the Scherrer equation of LnF₃ crystals.

For the first group (La−Sm), the products are all mainly composed of well-separated elongated nanoparticles. Simultaneously, there are a few round nanoparticles identified. Figure 2 shows the TEM images of LaF₃ (A), CeF₃ (B), PrF₃ (C), and NdF₃ (D) as well as SEM (E) and TEM (F) image of SmF₃. The sizes of particles are 34−150 nm in length
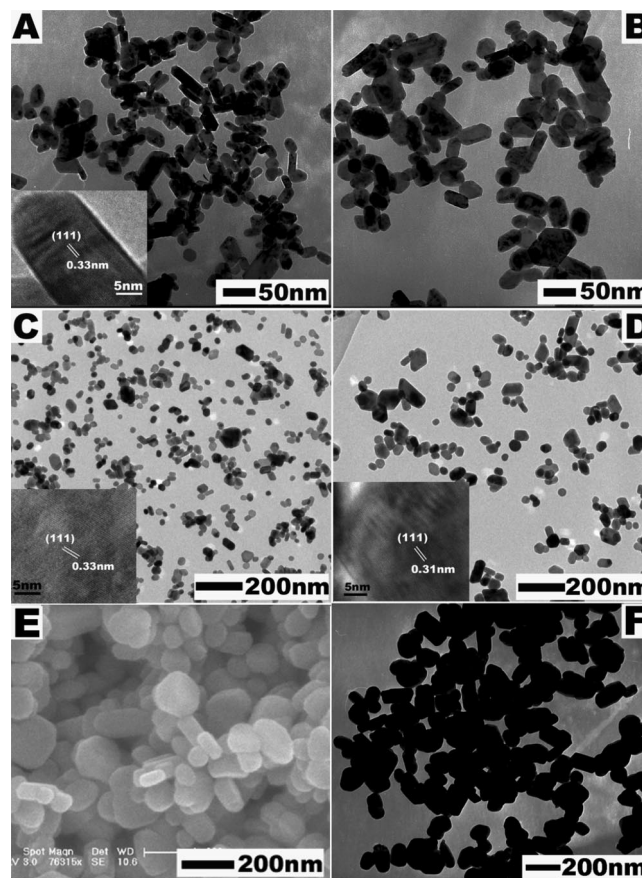
Figure 2. TEM and SEM images of LnF₃ (Ln = La to Sm) elongated nanoparticles. TEM images of (A) LaF₃, (B) CeF₃, (C) PrF₃, and (D) NdF₃ and SEM (E) and TEM (F) images of SmF₃. Insets in panels A, C, and D are HRTEM images of individual LaF₃, PrF₃, and NdF₃ nanoparticles, respectively.

(10) (a) Socrates, G. *Infrared and Raman Characteristic Group Frequencies*; John Wiley and Sons Ltd.: New York, 1999. (b) Xu, M.; Zhang, W. P.; Dong, N.; Jiang, Y.; Tao, Y.; Yin, M. *J. Solid State Chem.* **2005**, *178*, 477.
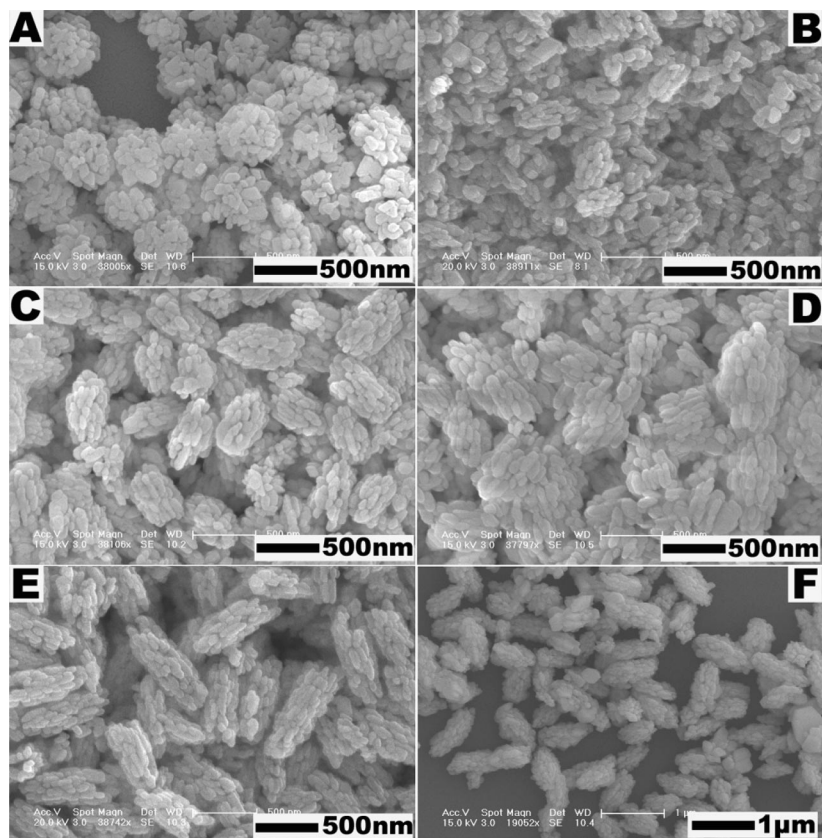
Figure 3. SEM images of (A) EuF$_3$, (B) GdF$_3$, (C) TbF$_3$, (D) DyF$_3$, (E) HoF$_3$, and (F) ErF$_3$ submicroparticles.
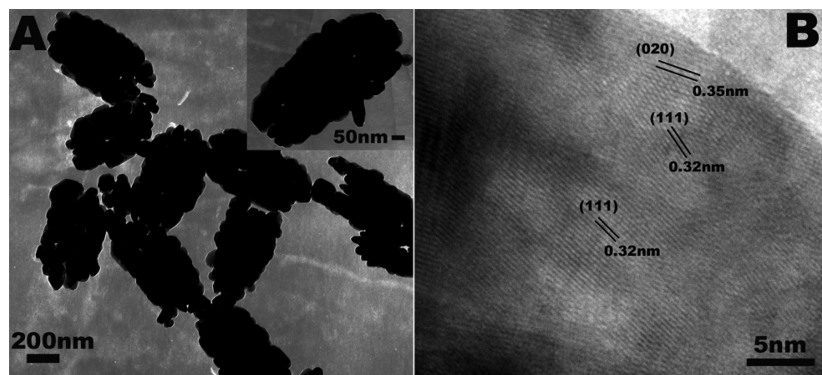
Figure 4. TEM (A) and HRTEM (B) images of TbF$_3$ spindle-like aggregates.

and 15−80 nm in diameter, as shown in Table 1. High-resolution TEM (HRTEM) observations can provide further insight into the nanoparticles. The insets in Figure 2A,C,D are the corresponding HRTEM images of LaF$_3$, PrF$_3$, and NdF$_3$, in which it can be clearly seen that the nanoparticles are structurally uniform with interplanar distances between adjacent lattice planes of about 0.33, 0.33, and 0.31 nm, corresponding to the *d*-spacing values of the (111) planes of the hexagonal phase of LnF$_3$.

For the second group (Eu to Er), the morphologies of all the samples are aggregates that consist of many even smaller nanoparticles with sizes of 10 to ∼30 nm, basically consistent with the results estimated from the Scherrer equation, $D = 0.941\lambda/\beta \cos \theta$, where D is the average grain size, λ is the X-ray wavelength (0.15405 nm), and θ and β are the diffraction angle and full-width at half-maximum (fwhm) of

an observed peak, respectively (as shown in Figure 3).[11] It is interesting to note that the shapes of the EuF$_3$ sample are almost submicrospheres with mean diameters of 560 nm (Figure 3A), while other LnF$_3$ (Gd to Er) samples are composed of uniform, highly monodisperse spindle-like aggregate particles. The even nanoparticles are in a special form of agglomeration; namely, they are slightly oblate in shape and self-assembled into ordered chains that are aligned approximately parallel to the spindle long axis. The aspect ratios of GdF$_3$ to ∼ErF$_3$ are 2.0, 1.7, 1.2, 6.0, and 2.2, respectively, as shown in Table 1. Structural information on the nanospindles was further afforded by TEM and HRTEM. For example, the TEM image of TbF$_3$ shows the obvious

(11) Wang, Z. L.; Quan, Z. W.; Jia, P. Y.; Lin, C. K.; Luo, Y.; Chen, Y.; Fang, J.; Zhou, W.; O'Connor, C. J.; Lin, J. *Chem. Mater.* **2006**, *18*, 2030.
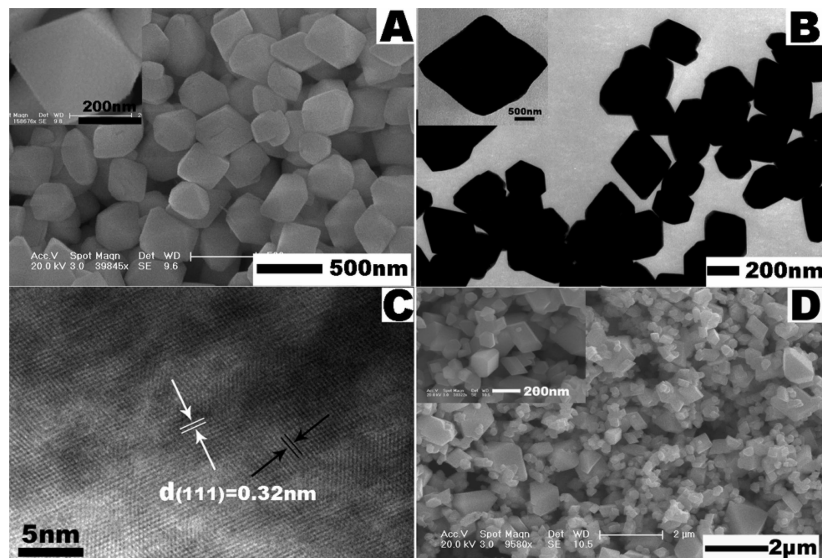
Figure 5. SEM and TEM images of as-prepared YbF_3 and LuF_3 samples. SEM (A), TEM (B), and HRTEM (C) images of YbF_3 and SEM (D) image of LuF_3.

spindle-like structure (Figure 4A). The HRTEM image for TbF_3 presents resolved fringe separations of about 0.35 and 0.32 nm, well coincident with distances of the (020) and (111) lattice planes of TbF_3, respectively (Figure 4B).

Conditions became quite different when we tried to grow YbF_3 and LuF_3 (the third group) with a similar method. For YbF_3, as shown in Figure 5A, polyhedral crystals with a mean size of around 350 nm are almost the exclusive products. The enlarged image (inset Figure 5A) clearly shows that those particles are in an octahedral morphology. Their surfaces are extremely smooth without obvious defects. Figure 5B shows the TEM images of the octahedra with various <110> and <111> orientations, in which rhombuses and small amounts of hexagons are the result of the incident electron beams parallel to the ξ and κ directions, respectively. The corresponding HRTEM image (Figure 5C) displays an interplanar distance of 0.32 nm, ascribed to the lattice spacing of the (111) planes of YbF_3, indicating the high crystallinity of the product. It is believed that the YbF_3 octahedra are bound by eight energetically equivalent {111} crystal facets, as those reported for Cu_2O and In_2O_3 octahedra, respectively.[12] As compared to YbF_3, the as-prepared LuF_3 sample shows a truncated octahedral shape with a not very uniform size distribution from 300 nm to 1 μm in edge length, as shown in Figure 5D.

Although the synthetic conditions are identical for all lanthanide ions, LnF_3 nano-/microcrystals with multiform structures and morphologies can be obtained. During crystal growth, organic additives are generally selectively adsorbed onto the different crystallographic facets of inorganic materials, consequently acting as a shape modifier and kinetically modulating the anisotropic growth of the crystals.[13] Cit^{3-}, a common organic additive, plays an important role in control-

ling the particle size and morphologies of the inorganic nanomaterials.[14] In addition, recent results demonstrated that different fluorine sources have strong impacts on the crystal phases and morphologies of rare earth fluorides.[15] Thus, in the following sections, we discuss the effects of Cit^{3-} and $NaBF_4$ on the crystal structures and morphologies of final products using La, Eu, and Lu as the representative rare earth elements among three groups. Moreover, the possible formation mechanisms for LnF_3 nano-/microcrystals with diverse morphologies as well as PL properties of Eu^{3+}-doped LnF_3 (Ln = La, Gd, and Lu) are presented.

Effect of Cit^{3-}. To validate the role of Cit^{3-}, a series of contrast experiments were conducted to fabricate LnF_3 in the absence of Cit^{3-} under the otherwise same reaction conditions. Note that the crystalline phases of the as-prepared products remain unchanged (Figure S2, Supporting Information); however, the corresponding morphologies (Figure 6) have a drastic change relative to those obtained in the presence of Cit^{3-} (Figures 2 and 5). Without Cit^{3-}, a typical TEM image of LaF_3 is presented in Figure 6A, which indicates that the product is also composed of elongated nanoparticles with the larger length of 48 nm with respect to that achieved in the presence of Cit^{3-}. The SEM image (Figure 6B) shows the general view of EuF_3 prepared under similar conditions, clearly indicating that the products consist of large-scale irregularly shaped particles. Meanwhile, the as-prepared LuF_3 sample has a regular and well-defined octahedral shape with an average edge length of about 10

(12) (a) Xu, H. L.; Wang, W. Z.; Zhu, W. *J. Phys. Chem. B* **2006**, *110*, 13829. (b) Hao, Y. F.; Meng, G. W.; Ye, C. H.; Zhang, L. D. *Cryst. Growth Des.* **2005**, *5*, 1617.

(13) (a) Sun, Y. G.; Xia, Y. N. *Science (Washington, DC, U.S.)* **2002**, *298*, 2176. (b) Li, C. C.; Shuford, K. L.; Park, Q. H.; Cai, W. P.; Li, Y.; Lee, E. J.; Cho, S. O. *Angew. Chem., Int. Ed.* **2007**, *46*, 3264.

(14) (a) Zhu, Y. F.; Fan, D. H.; Shen, W. Z. *J. Phys. Chem. C* **2007**, *111*, 18629. (b) Garcia, S. P.; Semancik, S. *Chem. Mater.* **2007**, *19*, 4016. (c) Li, H. B.; Chai, L. L.; Wang, X. Q.; Wu, X. Y.; Xi, G. C.; Liu, Y. K.; Qian, Y. T. *Cryst. Growth Des.* **2007**, *7*, 1918. (d) Sun, Y.; Zhang, L.; Zhou, H.; Zhu, Y.; Sutter, E.; Ji, Y.; Rafailovich, M. H.; Sokolov, J. C. *Chem. Mater.* **2007**, *19*, 2065. (e) Hu, J. Q.; Chen, Q.; Xie, Z. X.; Han, G. B.; Wang, R. H.; Ren, B.; Zhang, Y.; Yang, Z. L.; Tian, Z. Q. *Adv. Funct. Mater.* **2004**, *14*, 183.

(15) (a) Wang, M.; Huang, Q. L.; Hong, J. M.; Chen, X. T.; Xue, Z. L. *Cryst. Growth Des.* **2006**, *6*, 1972. (b) Wang, M.; Huang, Q. L.; Hong, J. M.; Chen, X. T.; Xue, Z. L. *Cryst. Growth Des.* **2006**, *6*, 2169. (c) Zhu, L.; Qin, L.; Liu, X. D.; Li, J. Y.; Zhang, Y. F.; Meng, J.; Cao, X. Q. *J. Phys. Chem. C* **2007**, *111*, 5898.
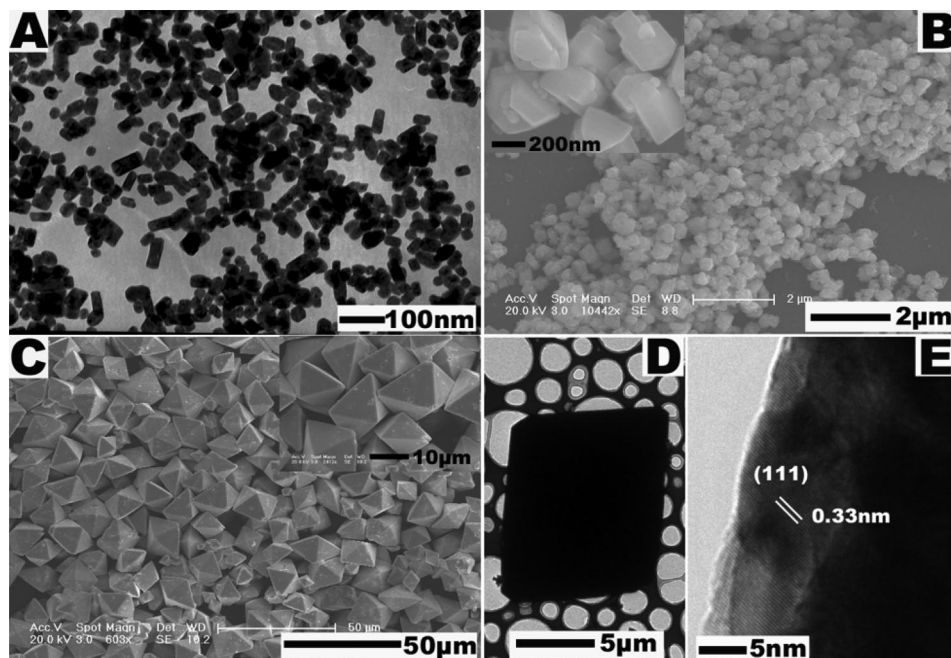
Figure 6. TEM and SEM images of as-prepared LnF_3 samples in the absence of Cit^{3-} under otherwise same reaction conditions. TEM image of LaF_3 (A), SEM image of EuF_3 (B), and SEM (C), TEM (D), and HRTEM (E) images of LuF_3.

μm (Figure 6C). More careful examination of the magnified SEM image (inset of Figure 6C) shows that the surfaces exhibit pores and small nanoparticles attached to them. Figure 6D shows the TEM image of an individual octahedron, in which a rhombic cross-section can be observed. The corresponding HRTEM image recorded on the tip of the rhombus indicates lattice fringes with interplanar spacings of 0.33 nm for the (111) planes of LuF_3, as illustrated in Figure 6E. The controllable experiments demonstrate that Cit^{3-} plays an important role in the morphology of the final products. For the first and third group fluorides, although the presence of Cit^{3-} has no obvious impact on the morphologies, the sizes of the crystals decrease significantly in comparison to those in the absence of Cit^{3-}. However, for the second group fluorides, Cit^{3-} affects remarkably the shape of the products. This means that the Cit^{3-} ions are selectively adsorbed on the different crystal facets of the growing particles and change the relative surface energy of different crystal facets, consequently influencing the growth rates along certain orientations. Furthermore, with the changing of center atoms and crystal structures, the absorption/desorption ability of Cit^{3-} on the different crystal facets changes greatly, leading to a morphological variation of the products.

Effect of $NaBF_4$. Here, we emphasized the crucial effect of $NaBF_4$ on the crystalline phases and morphologies of the products in our current synthesis. We used NaF as a F^- source to carry out contrastive experiments in an effort to reveal the unique role of $NaBF_4$ in determining LnF_3 products. Figure 7 shows the XRD patterns of the as-synthesized different products using NaF as the F^- source without changing the other parameters. For La, the structure still follows the LaF_3 hexagonal phase, but for Eu and Lu, Na^+ is incorporated into the matrix of Ln−F to form hexagonal (β)-NaEuF$_4$ and NaLuF$_4$. The morphologies of the corresponding products are shown in Figure 8. Figure
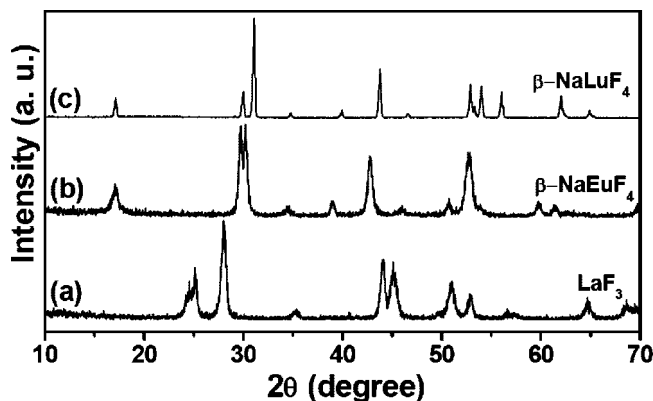
Figure 7. XRD patterns of as-prepared different products using NaF as the fluorine source under otherwise equal reaction conditions: (a) LaF_3, (b) β-NaEuF$_4$, and (c) β-NaLuF$_4$.

8A shows the formation of LaF_3 nanoplates (either lying flat on the faces or standing on the edges) in a mean thickness of 11 nm. Additionally, the shape of the as-obtained product is β-NaEuF$_4$ irregular nanoparticles (Figure 8B). In contrast, the general morphology of the β-NaLuF$_4$ product consists of uniform hexagonal microplates with an average diameter of 10 μm and a thickness of 0.8 μm (Figure 8C,D). Figure 8E is a TEM image of the product, which clearly shows very regular hexagonal cross-sections. In the corresponding HR-TEM image, taken with the electron beam perpendicular to the edge of the microplate, the interplayer distances between adjacent lattice fringes were determined to be 0.27 and 0.30 nm (Figure 8F), well-indexed as the d-spacing values of the ($20\bar{2}0$) and ($11\bar{2}0$) planes of the β-NaLuF$_4$ crystals, respectively. Our experiments further support this result that different fluorine sources have a tremendous effect on the morphologies of the final products. For LaF_3, independent of the F^- source, it preferred to segregate along with Na^+ in the solution, instead of forming NaLaF$_4$.[16] Conditions were
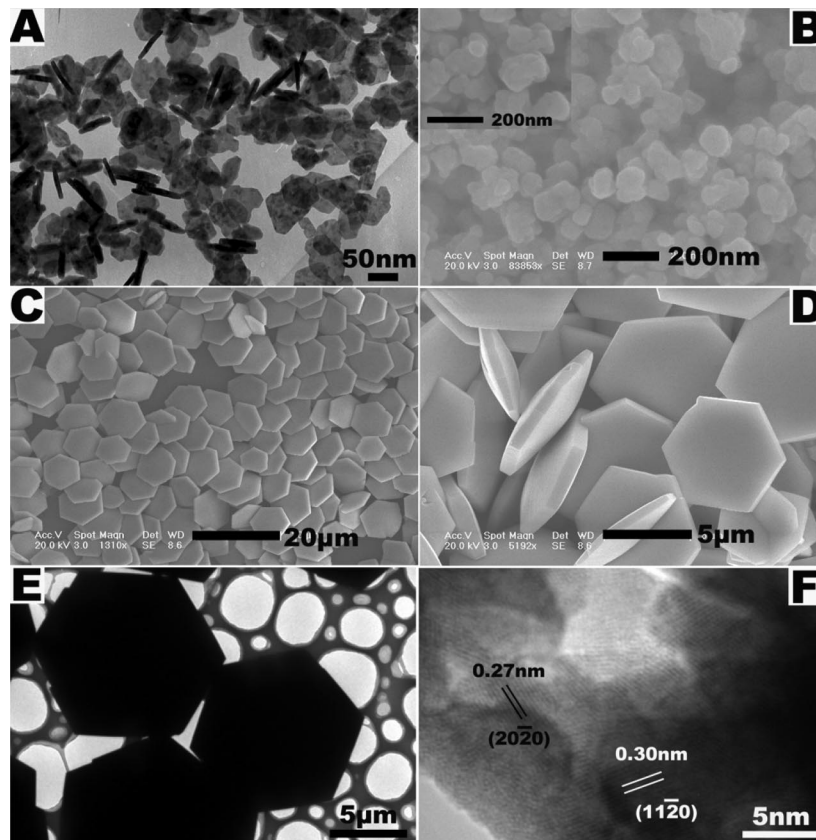
Figure 8. TEM and SEM images of as-prepared samples using NaF as the fluorine source under otherwise equal reaction conditions. TEM (A) image of LaF₃, SEM (B) image of β-NaEuF₄, and SEM (C and D), TEM (E), and HRTEM (F) images of β-NaLuF₄.

more complicated for Eu and Lu. When NaBF₄ acted as a F⁻ source, the initial solution was clear and transparent before hydrothermal treatment, suggesting that no fluoride precipitation formed. In this situation, at first, Cit^{3-} reacted with Ln^{3+} to form a $Ln^{3+}-Cit^{3-}$ complex through a coordination interaction (eq 1). On the other hand, in aqueous solution, NaBF₄ slowly was hydrolyzed to produce BO_3^{3-} and F⁻ anions, as shown in eq 2, which has been proven by other groups.[17] Especially in an acidic environment (pH 1), from the view of the reaction equilibrium, this situation is not favorable for the release of F⁻. Furthermore, the composition analysis of evaporating the clear solution after centrifugation demonstrates the formation of H_3BO_3 and $Na_2B_2O_4$ (eq 3).[18] Finally, Ln^{3+} released from the complexes reacted with F⁻ produced during the slow hydrolysis of NaBF₄ to form LnF₃ nuclei, as presented in eq 4. Because of the very low F⁻ concentration, the particle growth of the precipitated LnF₃ solid was very slow. The probable reaction processes for the formation of LnF₃ can be summarized as follows:

$$Ln^{3+} + Cit^{3-} \rightarrow Ln^{3+} - Cit^{3-} \text{ (complex)} \quad (1)$$

$$BF_4^- + 3H_2O \leftrightarrow 3HF + F^- + H_3BO_3 \quad (2)$$

$$2H_3BO_3 + Na^+ \rightarrow Na_2B_2O_4 + 2H_2O + 2H^+ \quad (3)$$

$$Ln^{3+} - Cit^{3-} + 3F^- \rightarrow LnF_3 + Cit^{3-} \quad (4)$$
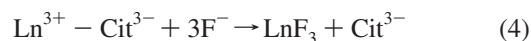
To further validate the fact that the strong acidic environment (pH 1) is advantageous to form the LnF₃ product, instead of NaLnF₄, we further examined the crystal phase of the products through changing the pH values of the initial solution. Our studies concerning lutetium fluorides indicated that if the pH value of the initial solution is not adjusted (pH 3), cubic phase (α-)NaLuF₄ is formed. However, if the pH value increases to 7, the product is hexagonal phase (β-)NaLuF₄, as shown in Figure S3 (Supporting Information). Only at strong acidic solutions (pH 1) can the LuF₃ crystal phase be obtained. Namely, in our current conditions, borate–sodium prevents the formation of NaLnF₄. But when NaF serves as the F⁻ source, the precursor solution is turbid before the hydrothermal treatment, indicating the formation of rare earth fluoride nuclei. In this case, NaF dissociates quickly to produce Na⁺ in aqueous solution. All F⁻ ions are available immediately. Under the hydrothermal conditions (high pressure and temperature), the Ln^{3+} released from the complexes very easily reacts with a high concentration of F⁻ and Na⁺ to form β-NaLnF₄ nuclei (Ln = Eu and Lu). As a consequence, for Eu and Lu, the use of different fluorine sources gives rise to significant structure transformation and morphology evolution of the products. From the previous analysis, we further affirmed the unique and crucial role of NaBF₄ in the formation of LnF₃ crystalline structures.

Possible Formation Mechanisms of LnF₃ Nano-/Microcrysals. For the first group (La to Sm), under the hydrothermal conditions, the LnF₃ nuclei formed initially

(16) Mai, H. X.; Zhang, Y. W.; Si, R.; Yan, Z. G.; Sun, L. D.; You, L. P.; Yan, C. H. *J. Am. Chem. Soc.* **2006**, *128*, 6426.

(17) (a) Miao, Z. J.; Liu, Z. M.; Ding, K. L.; Han, B. X.; Miao, S. D.; An, G. M. *Nanotechnology* **2007**, *18*, 125605. (b) Zhu, L.; Meng, J.; Cao, X. Q. *Eur. J. Inorg. Chem.* **2007**, 3863.

(18) Wang, M.; Huang, Q. L.; Zhong, H. X.; Chen, X. T.; Xue, Z. L.; You, X. Z. *Cryst. Growth Des.* **2007**, *7*, 2106.

Scheme 1. Possible Formation Mechanisms of LnF₃ Nano-/Microcrystals with Various Morphologies
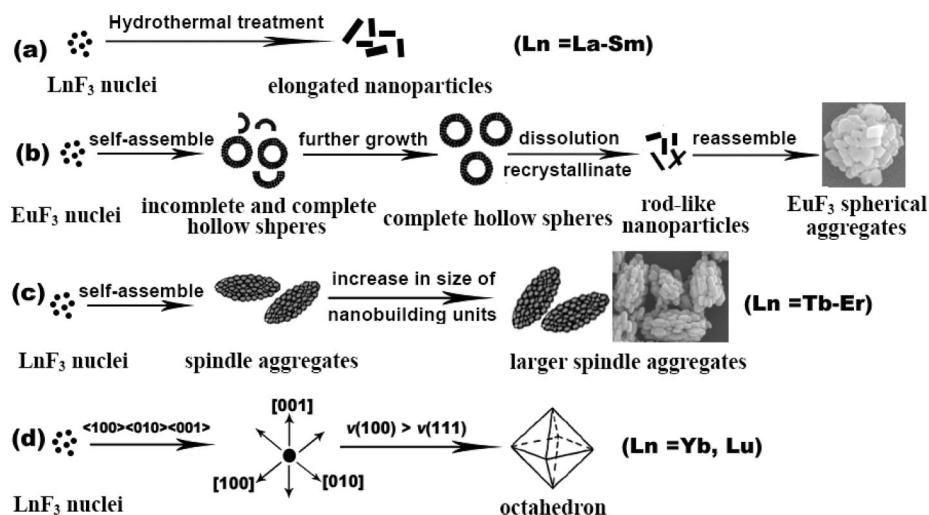
grew the elongated nanoparticles, as shown in Scheme 1a. For the second group (Eu to Er), because EuF₃ are spherical aggregates, which differ from the spindle-like aggregates of LnF₃ (Gd to Er), the growth mechanisms were investigated separately. We conducted a series of detailed time-dependent experiments to obtain intermediates, which were used to understand the shape evolution of the crystals. For EuF₃ spheres, TEM images of the corresponding intermediates prepared at the same hydrothermal temperature (180 °C) are shown in Figure 9. Interestingly, at $t = 15$ min, the tiny EuF₃ nuclei formed at the first stage were self-assembled into packed hollow spheres with a mean diameter of 360 nm accompanied by some incomplete hollow spheres (Figure 9A). With the reaction time up to 30 min, the dominant morphology of the products was nearly complete hollow spheres with an increased size of 500 nm. Simultaneously,

some nanoparticles began to appear, as shown in Figure 9B. After 6 h of growth, hollow spherical structures disappeared, while rod-like nanoparticles with a mean length of 100 nm and width of 27 nm almost became the exclusive products. Moreover, some nanoparticles were not monodisperse and interconnected (Figure 9C). This is a process of dissolution–recrystallization of EuF₃. Then, along with the increase of reaction time, these formed nanoparticles served as primary nanobuilding units to reassemble and rearrange in a three-dimensional array to form eventually uniform submicrospheres with an average diameter of 560 nm, as shown in Figure 9D. Additionally, because the nanoparticles packed compactly to form spherical structures, the nature of hollow interiors was hardly present. Scheme 1b shows the possible formation mechanism for the EuF₃ spherical aggregates. However, the formation mechanism of LnF₃ (Tb to Er)
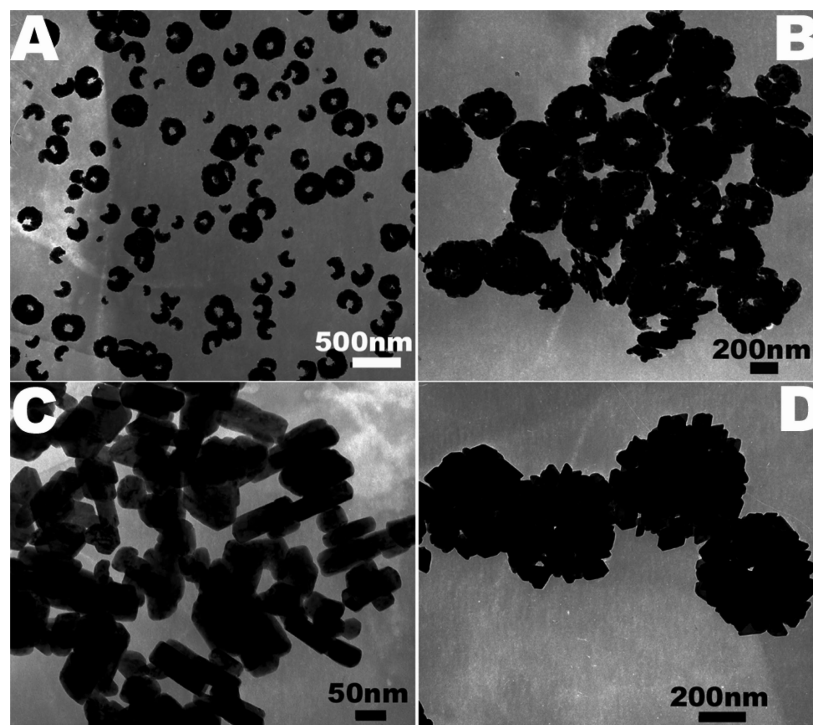
Figure 9. TEM images of EuF₃ products at 180 °C for different time intervals of (A) 15 min, (B) 30 min, (C) 6 h, and (D) 24 h.

spindle-like aggregates was completely different from that of EuF₃. By taking TbF₃ as a representative example, at $t = 30$ min, spindle-like structures formed with a homogeneous shape, as shown in Figure S4A (Supporting Information). The magnified image (inset of Figure S4A) shows that the products are also aggregates constructed from a large amount of nanoparticles. The length and diameter are 470 and 200 nm, respectively. With the reaction time extending to 4 and 24 h, there are no further changes in morphology except that the sizes of the particles become much bigger, as shown in Figure S4B,C, respectively. But, careful observations of the magnified images (inset in Figure 4SA−C) indicate that the nanobuilding unit-constructed aggregates increase gradually in size with the reaction proceeding. The possible formation mechanism for the LnF₃ (Tb−Er) spindle-like aggregates is shown in Scheme 1c. This mechanism is quite different from that of YF₃ nanospindles.[19] As for the formation of octahedral YbF₃ and LuF₃ bound by eight {111} surfaces, it is caused by the relatively enhanced growth rate along the <100> versus <111> directions. Furthermore, it has been demonstrated that the addition of simple salts can influence remarkably the morphology of the products.[20] In our adopted reaction system, the BO_3^{3-} and BF_4^{-} anions with a certain concentration in the solution may favor preferential crystal growth along the <100> direction and make it far exceed that of <111> thus, the {100} faces shrink. In general, facets perpendicular to the fast directions of growth have smaller surface areas, and slower growing facets therefore dominate the morphology.[21] The crystal morphology will be defined by the slowest {111} growing facets because the fastest {100} growing facets shrink, resulting in formation of the octahedral shape. In addition, Cit^{3-} can also be absorbed onto the specific crystal planes of octahedral crystals, consequently inhibiting the radical growth of these planes and leading to the much smaller size relative to that in the absence of Cit^{3-}. The whole formation process is shown in Scheme 1d.

PL Properties of Eu³⁺-Doped LnF₃ (Ln = La, Gd, and Lu). Lanthanide fluorides have been considered as ideal host lattices for optically active lanthanide ions, and different doping modes may lead to quite different emission behaviors, which are appealing to applications such as biological labeling and optics.[22] The luminescence of lanthanide ions originates from electron transitions within the 4f shells. Hence, in this work, the optical properties of 5 mol % Eu³⁺-doped LnF₃ (Ln = La, Gd, and Lu) samples are investigated in detail, and all the Eu³⁺ doped products were prepared by the same synthetic pathway. Note that this doping process alters neither the crystal structures nor the shapes of the host materials. Room temperature excitation and emission spectra for three samples are shown in Figure 10. It can be seen clearly that their excitation spectra exhibit some difference depending on Ln³⁺. The excitation spectra for LaF₃:Eu³⁺ (Figure 10a) and LuF₃:Eu³⁺ (Figure 10e) are identical. In general, most of the excitation lines can be clearly assigned
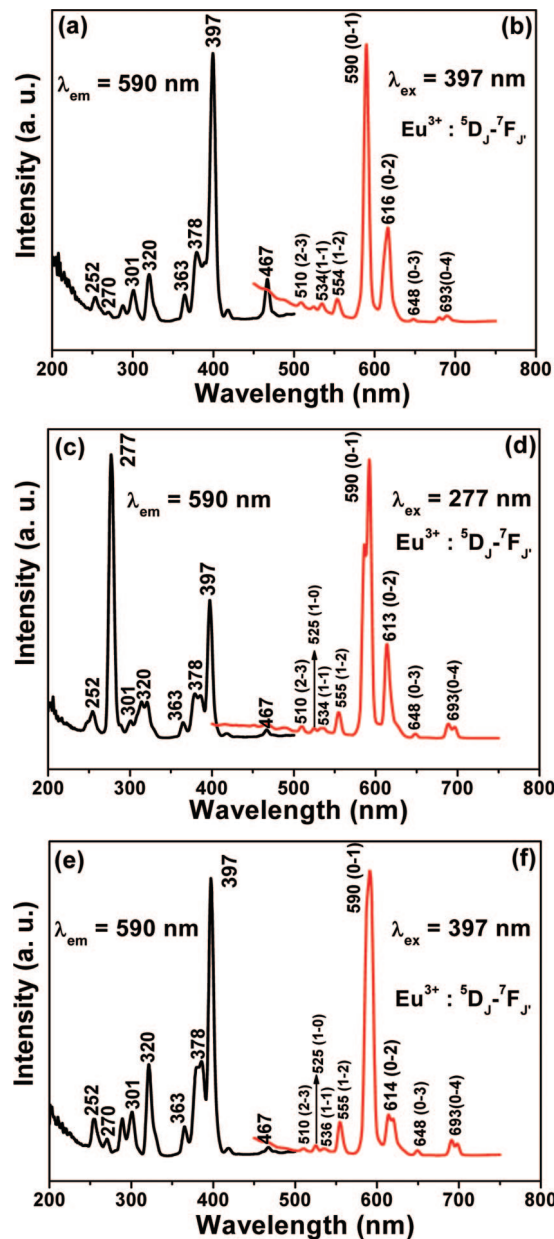
Figure 10. PL excitation and emission spectra of 5% Eu³⁺-doped LaF₃ (a and b), GdF₃ (c and d), and LuF₃ (e and f).

(320 nm: $^7F_0 \rightarrow {}^5H_6$; 363 nm: $^7F_0 \rightarrow {}^5D_4$; 378 nm: $^7F_0 \rightarrow {}^5G_2$; 397 nm: $^7F_0 \rightarrow {}^5L_6$, strongest; and 467 nm: $^7F_0 \rightarrow {}^5D_2$) except for those weak ones at 252, 270, and 301 nm (which have little contribution to the excitation of Eu³⁺ and are of minor significance).[23] In contrast, the excitation spectrum of GdF₃:Eu³⁺ is quite different, as presented in Figure 10c. The excitation peaks at 363, 378, and 397 nm originate from the transitions from the ground state $^7F_0$ level of Eu³⁺ to different excited states, similar to the cases of LaF₃:Eu³⁺ and LuF₃:Eu³⁺. But, the excitation peaks at 320 and 277 nm (strongest) originate from the transitions of $^8S_{7/2} \rightarrow {}^6P_J$ and $^8S_{7/2} \rightarrow {}^6I_J$ of Gd³⁺, respectively. Upon excitation into

(19) Zhang, M. F.; Fan, H.; Xi, B. J.; Wang, X. Y.; Dong, C.; Qian, Y. T. *J. Phys. Chem. C* **2007**, *111*, 6652.

(20) (a) Xia, T.; Li, Q.; Liu, X. D.; Meng, J.; Cao, X. Q. *J. Phys. Chem. B* **2006**, *110*, 2006. (b) Filankembo, A.; Pileni, M. P. *J. Phys. Chem. B* **2000**, *104*, 5865.

(21) Murphy, C. J. *Science (Washington, DC, U.S.)* **2002**, *298*, 2139.

(22) (a) Sivakumar, S.; van Veggel, F. C. J. M.; Stanley, M. P. *J. Am. Chem. Soc.* **2007**, *129*, 620. (b) Sudarsan, V.; Sivakumar, S.; van Veggel, F. C. J. M.; Raudsepp, M. *Chem. Mater.* **2005**, *17*, 4736. (c) Diamente, P. R.; Burke, R. D.; van Veggel, F. C. J. M. *Langmuir* **2006**, *22*, 1782.

(23) Deshazer, L. G.; Dieke, G. H. *J. Chem. Phys.* **1963**, *38*, 2190.

the $^8S_{7/2} \rightarrow {}^6I_J$ transition at 277 nm of Gd^{3+}, the obtained emission spectrum exhibits characteristic lines of Eu^{3+} (Figure 10d), and no emission from Gd^{3+} is observed. This indicates that an efficient energy transfer occurs from Gd^{3+} to Eu^{3+} in $GdF_3:Eu^{3+}$ as reported previously for $LiGdF_4$: Eu^{3+}.[24] However, the emission spectra (Figures 10b,d,f) of three samples are basically similar in shape; namely, they consist of a series of resolved the emission lines ranging from 500 to 750 nm associated with the Eu^{3+} transitions from the excited $^5D_{0,1,2}$ levels to the ^7F_J level ($J = 0-4$), with $^5D_0 \rightarrow {}^7F_1$ orange emission as the most prominent group. It is well-known that the symmetry of the crystal sites in which Eu^{3+} are located will determine the relative intensity of the $^5D_0 \rightarrow {}^7F_1$ and $^5D_0 \rightarrow {}^7F_2$ transitions. If Eu^{3+} is located at a site with inversion symmetry, the $^5D_0 \rightarrow {}^7F_1$ magnetic-dipole transition is dominant, otherwise (with noninversion symmetry), the $^5D_0 \rightarrow {}^7F_2$ electric-dipole transition is dominant.[25] In our case, the $^5D_0 \rightarrow {}^7F_1$ magnetic-dipole transition is the strongest in the three samples, indicating that the Eu^{3+} ion is located in the Ln^{3+} crystal sites with an inversion center (D_{6h} symmetry for hexagonal $LaF_3:Eu^{3+}$ and C_{2h} system for orthorhombic $GdF_3:Eu^{3+}$ and LuF_3: Eu^{3+}).[7] Meanwhile, the strong $^5D_0 \rightarrow {}^7F_1$ emission can also be ascribed to the fluoride host since any forced electric-dipole transitions require an allowed transition at relatively low energy to mix in with the $^5D_0$ state. Since these nanoparticles are fluorides, the allowed $Eu^{3+}-F^-$ charge transfer transition will be at exceedingly high energies, reducing the probability for forced electric-dipole ($^5D_0 \rightarrow {}_7F_2$) transitions, which has been pointed out by Blasse and Grabmaier in various hosts.[26] Finally, it is difficult to quantify the intensity differences between samples when the sample absorption is weak (as it is for 4f−4f absorption transitions in this case).

(24) Wegh, R. T.; Donker, H.; Oskam, K. D.; Meijerink, A. *Science (Washington, DC, U.S.)* **1999**, *283*, 663.
(25) Judd, B. R. *Phys. Rev.* **1962**, *127*, 750.
(26) Blasse, G.; Grabmaier, B. C. *Luminescence Materials*; Springer-Verlag: Berlin, 1994.

Conclusion

In conclusion, via a simple hydrothermal route, we demonstrated a general synthesis of LnF_3 crystals using water as the reaction medium. Three types of dominant morphologies were achieved (i.e., one is elongated nanoparticles (La to Sm), one is aggregates (Eu to Er), and another is octahedra (Yb and Lu)). The employment of $NaBF_4$ plays a unique and critical role in obtaining LnF_3 crystal structures. Cit^{3-} has an important influence on the shapes of the products to some degree. The possible formation mechanisms for LnF_3 nano-/microcrystals with diverse morphologies were presented in detail. The Eu^{3+}-doped LnF_3 (Ln = La, Gd, and Lu) samples show characteristic emission lines (500−750 nm) corresponding to transitions from the excited $^5D_{0,1,2}$ levels to the ^7F_J levels ($J = 0-4$) of Eu^{3+}, with $^5D_0 \rightarrow {}^7F_1$ orange emission as the most prominent group. Additionally, an efficient energy transfer took place from Gd^{3+} to Eu^{3+} in $GdF_3:Eu^{3+}$. These results not only enrich the contents of lanthanide fluoride chemistry but also provide fundamental insight into the crystal growth and formation mechanism of nano-/microscale materials.

Supporting Information Available: FT-IR spectrum of as-prepared LaF_3 sample (Figure S1), XRD patterns of as-prepared LnF_3 samples in the absence of Cit^{3-} under otherwise equal reaction conditions (Figure S2), XRD patterns of as-prepared different lutetium fluorides obtained at different pH values in a similar way to the preparation of LuF_3 (Figure S3), TEM images of TbF_3 products at 180 °C for different time intervals of (A) 30 min, (B) 4 h, and (C) 24 h (Figure S4) (PDF). This material is available free of charge via the Internet at http://pubs.acs.org.

CM800279H